UNIVERSITY OF LEEDS

This is a repository copy of *Simulated [111] Si-SiGe terahertz quantum cascade laser*.

White Rose Research Online URL for this paper:
http://eprints.whiterose.ac.uk/3632/

Article:

Lever, L., Valavanis, A., Ikonic, Z. et al. (1 more author) (2008) Simulated [111] Si-SiGe terahertz quantum cascade laser. Applied Physics Letters, 92 (2). 021124. ISSN 1077-3118

https://doi.org/10.1063/1.2836023

Reuse
See Attached

Takedown
If you consider content in White Rose Research Online to be in breach of UK law, please notify us by emailing eprints@whiterose.ac.uk including the URL of the record and the reason for the withdrawal request.

White Rose
university consortium
Universities of Leeds, Sheffield & York

eprints@whiterose.ac.uk
https://eprints.whiterose.ac.uk/

promoting access to White Rose research papers

White Rose
Research Online

Universities of Leeds, Sheffield and York
http://eprints.whiterose.ac.uk/

This is an author produced version of a paper published in **Applied Physics Letters**.

White Rose Research Online URL for this paper:
http://eprints.whiterose.ac.uk/3632/

Published paper

Lever, L., Valavanis, A., Ikonic, Z. and Kelsall, R. W. (2008) *Simulated [111] Si-SiGe terahertz quantum cascade laser.* Applied Physics Letters, 92 (2). 021124.
doi: 10.1063/1.2836023

White Rose Research Online
eprints@whiterose.ac.uk

Simulated [111] Si–SiGe THz Quantum Cascade Laser

L. Lever,* A. Valavanis, Z. Ikonić, and R. W. Kelsall
Institute of Microwaves and Photonics, School of Electronic and Electrical Engineering,
University of Leeds, Leeds LS2 9JT, United Kingdom
(Dated: February 13, 2008)

The prospect of developing a silicon laser has long been an elusive goal, mainly due to the indirect band-gap and large effective carrier masses. We present a design for a THz intersubband laser grown on the [111] crystal plane, and simulate performance using a rate equation method including scattering due to alloy disorder, interface roughness, carrier–phonon and Coulombic interactions. We predict gain greater than $40\,\mathrm{cm}^{-1}$ and a threshold current density of $70\,\mathrm{A/cm}^2$.

PACS numbers: 73.50.Bk, 73.21.Fg, 73.43.Cd, 73.61.Cw
Keywords: Silicon; Germanium; SiGe; QCL, quantum c

Quantum cascade lasers (QCLs) have undergone much development over recent years and are now commercially available as compact semiconductor sources of THz radiation. A Si-based THz QCL would potentially reduce fabrication costs because of the mature processing technology.[1] Intersubband electroluminescence has been demonstrated in Si–SiGe systems,[2, 3] however, an Si-based QCL has yet to be realized.

Investigation of Si–SiGe QCLs has so far focused on p-type systems grown on [100] Si substrates. The most commonly stated reasons are that valence band offsets are larger than conduction band offsets, that n-type dopants cannot be localized within individual barriers, and that hole masses are lower than the electron masses.[4] however, we will show that none of these cited drawbacks are an issue for [111] oriented n-type systems. Firstly, conduction band offsets were calculated to be 160 meV for Si–$\mathrm{Si_{0.5}Ge_{0.5}}$ on [111] strain-symmetrized virtual substrates, which is certainly large enough for THz intersubband transitions. Secondly, our calculated ionized impurity scattering for uniformly distributed dopants does not significantly affect the carrier dynamics. Finally, the quantization mass for the [111] orientation is approximately equal to the heavy-hole mass.

Designs have emerged for n-type Si-based QCLs exploiting L-valley transitions in Ge–SiGe systems,[5, 6] however these require very high Ge fraction virtual substrates which are difficult to grow on an Si substrate. Some progress has been made towards an n-type QCL using Si–SiGe in the [100] orientation,[7] but the many-valley band structure causes problems. The conduction band minima are in the six degenerate Δ valleys in bulk materials. However, strain and effective mass anisotropy split the degeneracy in QCLs into a pair of $\Delta_\perp$ valleys with quantization effective mass, $m_q = 0.916$ (the longitudinal effective mass) and a quartet of $\Delta_\parallel$ valleys with $m_q = 0.19$ (the transverse effective mass). In [111], the quantization effective mass, $m_q = 0.26$, is the geometric mean of the longitudinal and transverse effective masses[8] (*c.f.* heavy-hole masses of 0.29 in Si and 0.21 in Ge).[9]

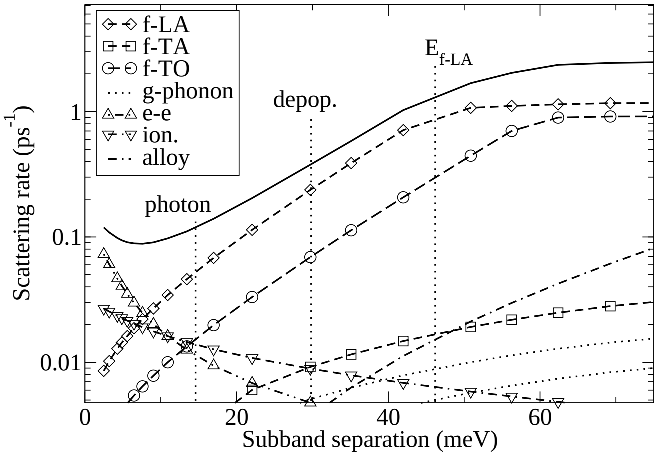

FIG. 1: Intersubband scattering rates as a function of subband energy separation at 4 K lattice temperature and 150 K electron temperature. For most energies, f-type phonon-interactions dominate, particularly the f-LA phonon process. There is a minimum at around 10 meV, below which carrier–carrier scattering dominates.

In [100], the $\Delta_\perp$ band offset is larger, and the subband energies lower than the $\Delta_\parallel$ case.[10] The $\Delta_\parallel$ states are effectively unconfined for quantum wells (QWs) on length scales that strongly confine the $\Delta_\perp$ states. A similar situation exists with light-hole states in [100] p-type systems. In these anisotropic mass systems, the energy range for intersubband transitions is limited by strain-splitting to avoid populating the low mass states. Using thicker barriers increases the splitting but reduces the dipole matrix element between QWs. Growth in the [111] orientation preserves the Δ valley degeneracy, and thus avoids these constraints. Although the band offset is lower than those of the high mass states in [100] systems, the usable energy range for intersubband transitions increases as it is no longer restricted by the presence of low mass states. Conduction band offsets were calculated using the model solid approximation.[11] Δ minima were located for unstrained alloys by interpolation of elemental $\Gamma \to \Delta$ band

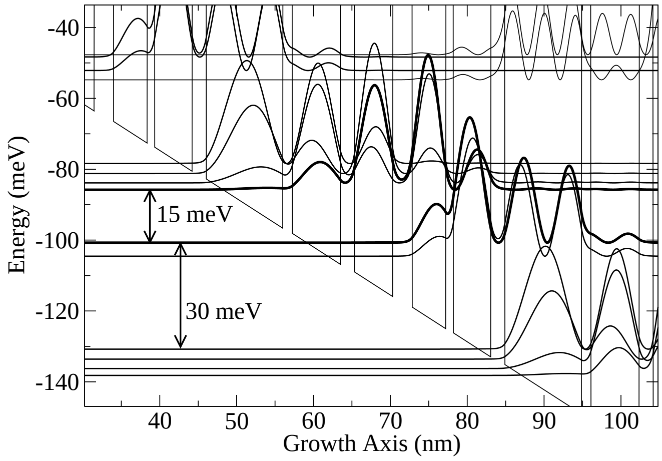

FIG. 2: Electron location probabilities at the design bias of 13.5 kV/cm. The 15 meV transition gives optical emission at 3.6 THz. The barrier dimensions (in nm) are: **6.3**, 1.8, **5.0**, 2.5, **4.4**, 0.9, **4.9**, 1.8, **10.0** 1.2 with the Si wells in bold. Dopants are spread uniformly throughout the structure at a density of $2{\times}10^{16}$ cm^{-3}.

gaps[12] and valence band maxima.[10] Strain components were calculated along the growth axes and transformed to the principal crystallographic axes.[13] Energy shifting due to hydrostatic strain was included by multiplying the trace of the strain tensor by the conduction band hydrostatic strain deformation potential.[11]

State populations were calculated by solving a set of rate equations[14] for the quatum confined states, accounting for alloy disorder,[15] ionised impurity,[15] intravalley acoustic phonon processes,[15] interface roughness,[16] intervalley electron–phonon[17] and carrier–carrier scattering.[18] Gain,[19] electroluminescence[18] and current density[19] were then calculated using the subband populations obtained from the solutions of the rate equations. Further detail on the [111] Si–SiGe heterostructure carrier-dynamics is given in our related publication.[20]

To gain insight into the carrier dynamics in [111] n-type systems, intersubband scattering rates between the first excited state and the ground state in a single QW are plotted in Fig 1 as a function of subband energy separation. The total scattering rate is lowest at around 10 meV subband separation and increases approximately exponentially as the subbands separate further. Below 10 meV separation, the fastest process is carrier–carrier scattering. At higher separations, f-LA phonon interactions dominate.

The electron probability densities at the design bias are shown in Fig 2. The design exploits the dependence of scattering on subband separation by having a radiative transition at 15 meV and a depopulation transition of 30 meV. Although a larger depopulation energy would enhance depopulation, it would require an increased electric field and hence give rise to a larger current and higher electron temperatures. 30 meV was chosen as a compromise between these factors.

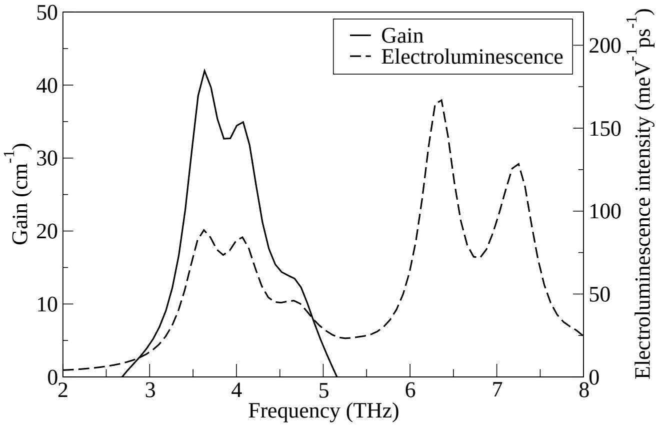

FIG. 3: Gain and electroluminescence at 13.5 kV/cm. The gain peak at 3.6 THz corresponds to the designated laser transition, and the additional peak at 4 THz corresponds to stimulated transitions into the subband just below the lower laser level. Absorption below 2 THz is due to intra-miniband transitions and at 6–8 THz due to transitions across the large depopulation well. Spontaneous emission occurs at the same frequencies as stimulated emission and at energies corresponding to the depopulation transitions in the large well.

Electron temperatures were calculated self-consistently[19] to be 150±10 K at the design bias and at a lattice temperature of 4 K. The doping was $2{\times}10^{16}$ cm^{-3} throughout the system, giving $7.8{\times}10^{10}$ cm^{-2} sheet density, which is low enough to avoid significant band-bending due to space-charge.

The carrier lifetimes were calculated as 6.11 ps for the upper laser level and 2.74 ps for the lower laser level, and the population inversion was 17.9 % of the sheet doping density. Fig 3 shows the gain and electroluminescence at the design bias. A 41 cm^{-1} gain peak occurs at 3.6 THz and a slightly smaller one at 4.0 THz resulting from the transition between the upper laser level and the level directly below the lower laser level. There are large intraminiband absorptions around 0–2 THz, and absorptions at 6–8 THz due to transitions from the ground state to both the lower laser level and extraction level. Gain first appears at 10 kV/cm, with a frequency of 2.9 THz, and persists until 15 kV/cm where it has shifted to 4.0 THz. Spontaneous emission peaks coincide with the stimulated emission energies, with two additional higher frequency peaks for the depopulation transitions in the large well.

Current density as a function of electric field is shown in Fig 4. There is some noise in the region 13–15 kV/cm, which results from the energy dependence of the scattering rates and the lack of broadening of state energies in the simulation, however we see a break in alignment at around 15 kV/cm. We require the active region gain times the modal overlap to exceed the sum of the waveg-

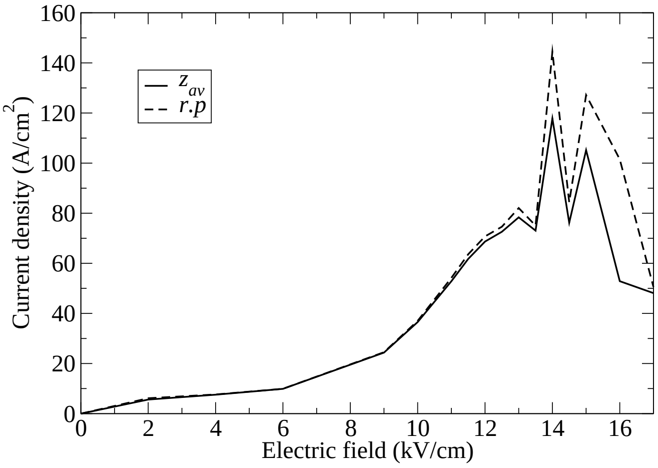

FIG. 4: Current density as a function of applied electric field. z_{av} is the current calculated according to the difference in z-expectation values between states, whereas $r.p$ is calculated by considering only inter-period scatterings across a 'reference plane' with an effective displacement of one period length.

uide and mirror losses in order to achieve lasing. Modelling of double plasmon THz Si waveguides indicate that we can expect waveguide losses of around $18\,\mathrm{cm}^{-1}$,[21] and we can expect mirror losses to be around $2\,\mathrm{cm}^{-1}$.[22] The gain exceeds this at around 12 kV/cm, from which we can infer that the threshold current density will be approximately $70\,\mathrm{A/cm}^2$. For a device area of $200\,\mu$m by 3 mm this corresponds to a current of 0.4 A, and for an active region height of $10\,\mu$m (and hence an applied bias of 12 V) we have a total dissipated power of 5 W assuming negligible contact resistance.

In conclusion, the [111] n-type system removes the design constraints imposed by the presence of low mass strain-split states in [100] systems, and as such is a more attractive candidate for Si-based QCLs. We have simulated Si–SiGe heterostructures on the [111] crystal plane using a rate equation approach which includes scattering due to phonons, interface roughness, alloy disorder and Coulombic interactions. Using this, we have developed a 3.6 THz Si–SiGe QCL design, with gain of over $40\,\mathrm{cm}^{-1}$ and a threshold current density of around $70\,\mathrm{A/cm}^2$.

---

[*] Electronic address: `l.j.m.lever@leeds.ac.uk`

[1] L. Pavesi, *Towards the First Silicon Laser* (Kluwer Academic Publishers, 2003).
[2] G. Dehlinger, L. Diehl, U. Gennser, J. Sigg, J. Faist, K. Ensslin, D. Grutzmacher, and E. Muller, Science **290**, 2277 (2000).
[3] R. Bates, S. A. Lynch, D. J. Paul, Z. Ikonić, R. W. Kelsall, P. Harrison, S. L. Liew, D. J. Norris, A. G. Cullis, W. R. Tribe, et al., Appl. Phys. Lett. **83**, 4092 (2003).
[4] R. W. Kelsall and R. A. Soref, Int. J. High Speed Electron. Syst. **13**, 547 (2003).
[5] K. Driscoll and R. Paiella, Appl. Phys. Lett. **89**, 191110 (2006).
[6] G. Sun, H. H. Cheng, J. Menéndez, J. B. Khurgin, and R. A. Soref, Appl. Phys. Lett. **90**, 251105 (2007).
[7] J. Lumin. **121**, 311 (2006).
[8] A. Rahman, M. S. Lundstrom, and A. W. Ghosh, J. Appl. Phys. **97**, 053702 (2005).
[9] M. Kahan, M. Chi, and L. Friedman, J. Appl. Phys. **75**, 8012 (1994).
[10] M. M. Rieger and P. Vogl, Phys. Rev. B **48**, 14276 (1993).
[11] C. G. Van de Walle, Phys. Rev. B **39**, 1871 (1989).
[12] J. Weber and M. I. Alonso, Phys. Rev. B **40**, 5683 (1989).
[13] S. Smirnov and H. Kosina, Solid-State Electron. **48**, 1325 (2004).
[14] Z. Ikonic, P. Harrison, and R. W. Kelsall, J. Appl. Phys. **96**, 6803 (2004).
[15] T. Unuma, M. Yoshita, T. Noda, H. Sakaki, and H. Akiyama, J. Appl. Phys. **93**, 1586 (2003).
[16] M. Califano, N. Q. Vinh, P. J. Phillips, Z. Ikonic, R. W. Kelsall, P. Harrison, C. R. Pidgeon, B. N. Murdin, D. J. Paul, P. Townsend, et al., Phys. Rev. B **75**, 045338 (pages 6) (2007).
[17] F. Monsef, P. Dollfus, S. Galdin, and A. Bournel, Phys. Rev. B **65**, 212304 (2002).
[18] P. Harrison, *Quantum Wells, Wires and Dots: Theoretical and Computational Physics of Semiconductor Nanostructures* (Wiley, Chichester, 2005), 2nd ed.
[19] V. D. Jovanovic, S. Hofling, D. Indjin, N. Vukmirovic, Z. Ikonic, P. Harrison, J. P. Reithmaier, and A. Forchel, J. Appl. Phys. **99**, 103106 (pages 9) (2006).
[20] A. Valavanis, Z. Ikonić, and R. W. Kelsall (2007).
[21] R. W. K. Z Ikonic and P. Harrison, Semicond. Sci. Technol. **19**, 76 (2004).
[22] B. S. Williams, Nat. Photonics **1**, 517 (2007).